



HAL
open science

A Supercooled Water Cloud Detection Algorithm Using Himawari-8 Satellite Measurements

Ziming Wang, Husi Letu, Huazhe Shang, Chuanfeng Zhao, Jiming Li, Run Ma

► **To cite this version:**

Ziming Wang, Husi Letu, Huazhe Shang, Chuanfeng Zhao, Jiming Li, et al.. A Supercooled Water Cloud Detection Algorithm Using Himawari-8 Satellite Measurements. *Journal of Geophysical Research: Atmospheres*, 2019, 124, pp.2724-2738. <10.1029/2018JD029784>. <insu-03686280>

HAL Id: insu-03686280

<https://insu.hal.science/insu-03686280v1>

Submitted on 3 Jun 2022

HAL is a multi-disciplinary open access archive for the deposit and dissemination of scientific research documents, whether they are published or not. The documents may come from teaching and research institutions in France or abroad, or from public or private research centers.

L'archive ouverte pluridisciplinaire **HAL**, est destinée au dépôt et à la diffusion de documents scientifiques de niveau recherche, publiés ou non, émanant des établissements d'enseignement et de recherche français ou étrangers, des laboratoires publics ou privés.



Distributed under a Creative Commons CC BY-NC-SA 4.0 - Attribution - Non-commercial use - ShareAlike - International License

A Supercooled Water Cloud Detection Algorithm Using Himawari-8 Satellite Measurements

**Key Points:**

- We developed a supercooled water cloud detection algorithm using high-resolution Himawari-8 satellite measurements
- Cloud effective radius and cloud phase tests are effective for detecting supercooled water clouds (SWCs)
- The SWC results of our algorithm well agree with lidar measurements in different seasons

Ziming Wang^{1,2} , Husi Letu¹ , Huazhe Shang^{1,3} , Chuanfeng Zhao⁴ , Jiming Li⁵ , and Run Ma^{1,6} 

¹State Key Laboratory of Remote Sensing Science, Institute of Remote Sensing and Digital Earth, Chinese Academy of Sciences, Beijing, China, ²School of Electronic, Electrical and Communication Engineering, University of Chinese Academy of Sciences, Beijing, China, ³Laboratoire d'Optique Atmosphérique, UMR 8518, Université de Lille1-Sciences et Technologies, CNRS, Lille, France, ⁴College of Global Change and Earth System Science, Beijing Normal University, Beijing, China, ⁵Key Laboratory for Semi-Arid Climate Change of the Ministry of Education, College of Atmospheric Sciences, Lanzhou University, Lanzhou, China, ⁶College of Resources and Environment, University of Chinese Academy of Sciences, Beijing, China

Correspondence to:

H. Letu,
husiletu@radi.ac.cn

Citation:

Wang, Z., Letu, H., Shang, H., Zhao, C., Li, J., & Ma, R. (2019). A supercooled water cloud detection algorithm using Himawari-8 satellite measurements. *Journal of Geophysical Research: Atmospheres*, 124, 2724–2738. <https://doi.org/10.1029/2018JD029784>

Received 9 OCT 2018

Accepted 10 FEB 2019

Accepted article online 14 FEB 2019

Published online 5 MAR 2019

Abstract The detection of supercooled water clouds (SWCs) is essential for artificial rain enhancement, the prevention of aircraft ice accretion, and better understanding of radiative energy balance. However, it is challenging to identify SWCs using only passive satellite measurements. We adopt measurements from the Advanced Himawari Imager, which is onboard the new-generation, high temporal, spatial, and spectral resolution geostationary Himawari-8 satellite, to develop a time-continuous Himawari-8 SWC (HSWC) algorithm. The HSWC algorithm includes a group of tests using comprehensive cloud properties (e.g., cloud phase [CPH], cloud top temperature, cloud optical thickness, and cloud effective radius [CER]). Unlike previous SWC detection algorithms, which are based on cloud top temperature and cloud optical thickness properties, we introduce CER and CPH information into the HSWC algorithm because the distribution of SWCs is sensitive to CER values, and SWCs may appear in mixed-phase clouds identified by satellites. Our analyses indicate that the additions of the CER and CPH tests could improve the performance of SWC detection by 15.07% and 4.75%, respectively. The full disk SWC detection results identified by the HSWC algorithm in January, May, August, and October of 2017 are validated using lidar measurements. The hit rate and false alarm rate are 93.52% and 25.27%, respectively. Our study provides potential SWC regions for the implementation of artificial rain enhancement.

1. Introduction

Cloud droplets, with a temperature below 0 °C, form supercooled water clouds (SWCs; Murray et al., 2012), which affect the radiative energy balance of the atmosphere and cause aircraft icing hazards (Cober et al., 2001). The latter, which involve the deposition or coating of ice on an airplane, can lead to excessive weight and drag, loss of lift, and even loss of control of the aircraft (Bellucci et al., 2007; Smith et al., 2012). A high frequency of mixed-phase clouds has been found with temperatures below 0 °C, which implies the global importance of SWCs. For example, approximately 30–40% of mixed-phase clouds have been found in the Arctic (Garrett & Zhao, 2006; Zhao & Garrett, 2015; Zhao et al., 2012). The detection of SWCs is also essential in guiding artificial rainfall (Wakimizu et al., 2002).

The SWC distribution can be derived from ground-based radar observations, airborne probes, and active airborne or spaceborne measurements (Choi et al., 2010; Hogan et al., 2004; Westbrook & Illingworth, 2011). Ground-based radars are efficient in detecting SWCs with a high temporal resolution (Hogan et al., 2003). From two case studies during the 1998 Cloud Lidar and Radar Experiment (CLARE'98) that observed mixed-phase clouds, 18 months of near-continuous ground-based lidar data from midlatitudes were used to show that SWCs occurred as a function of temperature (Hogan et al., 2003). However, it is difficult to monitor the SWC distribution at large spatial scales.

In two passive airborne observations via field campaigns by the National Aeronautics and Space Administration (i.e., the Polari meter Definition Experiment [PODEX], Studies of Emissions and Atmospheric Composition and the Clouds and Climate Coupling by Regional Surveys [SEAC4RS]), the Research Scanning Polari meter (RSP) loaded onto the ER-2 aircraft facilitated SWC observations with

©2019. The Authors.

This is an open access article under the terms of the Creative Commons Attribution-NonCommercial-NoDerivs License, which permits use and distribution in any medium, provided the original work is properly cited, the use is non-commercial and no modifications or adaptations are made.

very high polar metric accuracy (0.2% polarized degree; Alexandrov et al., 2016). For active airborne observations, Luke et al. (2010) proposed a method to detect SWCs by using morphological features in millimeter wavelength cloud radar Doppler spectra. Hogan et al. (2004) used the Lidar In-space Technology Experiment (LITE) highly backscattering profiles to distinguish SWCs from ice clouds. However, high-level ice clouds reduced the backscattering coefficients, which caused the underestimation of lower-level SWC frequency. Airborne remote sensing is important for selecting artificial rainfall times for a specific area and sampling data to validate the SWC detection algorithm. However, airborne measurements are rare.

Satellite remote sensing can observe a wide range of cloud microphysical properties from space. In active spaceborne remote sensing, by combining the cloud temperature estimated from the Goddard Earth Observing System-5 (GEOS-5) model with cloud height and phase information from Cloud-Aerosol Lidar and Infrared Pathfinder Satellite Observations (CALIPSO), Hu et al. (2010) further compiled global statistics regarding the occurrence, liquid water content (LWC), and SWC fractions and analyzed the relationship between SWCs and cloud top temperature (CTT). It was reported that the accuracy of the new results from the CALIPSO data achieved using the proposed method improved significantly from the previous results (Lin & Rossow, 1996; Weidle & Wernli, 2008). Although active remote sensing, such as CALIPSO, has an obvious advantage of providing cloud phase (CPH) information in the vertical direction by using depolarization ratio and layer-integrated backscatter intensity measurements (Hu et al., 2007, 2009), it is difficult to observe cloud cover over a wide area or with a high temporal resolution, similar to passive satellite sensors (Wang & Zhao, 2017; Zhang et al., 2010).

For passive spaceborne observations, Lin et al. (1998) proposed a method to detect SWCs from Tropical Rainfall Measuring Mission Microwave Imager 37-GHz measurements (specifically, supercooled water under other cloud layers) because microwaves can penetrate thick clouds. Roskovensky et al. (2011) analyzed the sensitivity of SWCs to cloud microphysical and thermodynamic properties from Moderate Resolution Imaging Spectroradiometer (MODIS) data and developed an SWC content detection algorithm, with uncertainties up to approximately 30% due to individual changes in cloud properties and corrections in the cloud water path. With the development of satellite remote sensing technology, geostationary satellites provide an opportunity for the continuous and widespread recognition of potential SWCs (Lin et al., 1998; Yao et al., 2018).

Ellrod and Nelson (1996) presented the potential for using geostationary satellite data to detect SWCs. Smith et al. (2000) proposed an algorithm, with the CTT situated between 273 and 233 K, to detect SWCs via the Geostationary Operational Environmental Satellites-8 (GOES-8) satellite. Pavolonis (2010) developed an SWC detection method by taking opaque cloud temperatures between 273.16 and 170.0 K as SWCs for a new generation of GOES-R. SWCs may appear in optically thick clouds, while the cloud optical thickness (COT) is not considered in this algorithm. According to the flowchart, this algorithm eliminates mixed-phase clouds and distinguishes SWCs from warm, liquid-phase clouds (Pavolonis, 2010). SWCs exist in the mixed phase according to the heterogeneous freezing theory (Pruppacher & Klett, 1997). This method does not use the characteristic that the distribution of SWCs is sensitive to cloud effective radius (CER) values (Baran et al., 2003). SWC detection algorithms for passive satellites in the above research have used the CTT and COT in liquid-phase clouds to detect SWCs, which does not consider the conditions of the CER and mixed-phase clouds.

In this study, we use not only the CTT and COT but also the CER and CPH from the Advanced Himawari Imager (AHI) level 2 product to develop the Himawari-8 SWC (HSWC) algorithm to detect SWCs for meteorological and disaster prediction applications. Detailed information about the data is presented in section 2. The HSWC algorithm and verified method are summarized in section 3. The sensitivity analysis on the validity of the CER and mixed-phase clouds in the CPH tests, the algorithm results, and a comparison with the CALIPSO observations are presented in section 4. Finally, a brief summary and conclusions are provided in section 5.

2. Data Sources

2.1. AHI Cloud Products

AHI cloud products are provided at a spatial resolution of 5 km, with a short time interval of approximately 10 min for full disk observations (from 60°S to 60°N and 80°E to 160°W within Figure 1; Bessho et al.,

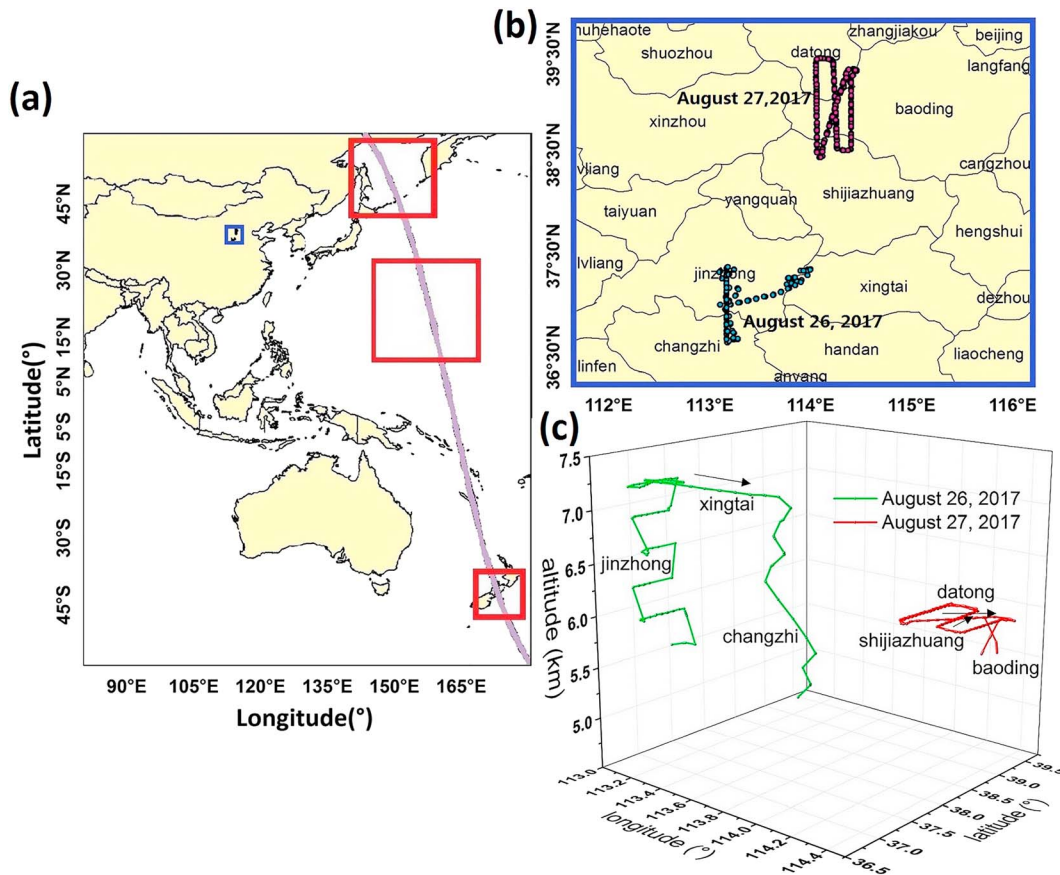


Figure 1. Study area. In Figure 1a, the blue box detailed depicted in Figure 1b represents areas of interest in section 2.2; the purple dashed line represents the Cloud-Aerosol Lidar with Orthogonal Polarization orbit track, and the red boxes denote the validation regions of high-latitude regions, ocean and land of Figure 4. In Figure 1c, specific flight tracks horizontally and vertically of the airborne measurements on 26 and 27 August 2017 from section 2.2 are depicted as the green and red tracks, respectively.

2016). The CPH products are determined using the brightness temperatures at 8.6 and 11.2 μm , the difference between these values, and the reflectance ratio $R(0.64 \mu\text{m})/R(1.6 \mu\text{m})$. Each pixel is divided into one of three CPHs, including (1) ice, (2) water, and (3) unknown or mixed phases. The CTT products are determined using the brightness temperature of 11 μm and temperature profiles of reanalysis data. The processes of this retrieval consider the information on ground and cloud thermal radiation (Nakajima & Nakajima, 1995). Optical CTT retrieval accuracy is influenced by misclassified cloud types, such as semitransparent clouds misclassified as opaque. Voronoi ice scattering model is used to retrieve the microphysical properties of ice- and mixed-phase clouds (Letu et al., 2016, 2018). The CER products retrieved at 2.3 μm by the AHI further retain the properties below the cloud top (Baran et al., 2003; King et al., 1997; Letu et al., 2018; Nakajima et al., 2010a, 2010b). The reflectance channel in AHI is effective for retrieving COT products (Letu et al., 2014). Its retrieval also includes the effect of thermal emissions and vertical water vapor profiles (Kawamoto et al., 2001). In the HSWC algorithm, the CPH products are used to identify liquid and mixed phases. The CTT, CER, and COT products are further used to detect SWCs.

2.2. Airborne Measurements of SWCs

The airborne measurements used for developing the statistics of the SWC droplet size distribution are derived from two flights on the border of the Hebei and Shanxi Provinces by the Chinese Academy of Meteorological Science (Figure 1). During the first flight, the aircraft flew above Jinzhong, Xingtai, and Changzhi between 09:02 and 11:03 UTC on 26 August 2017. The second flight was over Shijiazhuang, Baoding, and Datong on 27 August 2017, between 09:36 and 13:03 UTC at a stable flight altitude of

approximately 5.9 km. The Particle Measuring System probes onboard the aircraft are used to collect the LWC, cloud temperature, size distribution of particles, and other cloud microphysical information, which are described in detail by Houze et al. (1979) and Zhao et al. (2018). Based on experience when using airborne measurements, we recognize cloud droplets with temperatures below 0 °C, while LWCs higher than 10^{-3} g/m³ indicate SWCs (Reisner et al., 1998).

2.3. Cloud Layer Products

The midlayer height and temperature measurements from the Cloud-Aerosol Lidar with Orthogonal Polarization (CALIOP) cloud layer products are used to validate the HSWC algorithm results. The cloud layer products provide information about the spatial and optical characteristics of a feature, including the midlayer temperature and layer altitudes. This information is used to select the appropriate midlayer cloud temperature results for comparison with our results. The layer altitudes are estimated from the vertical profiles of total backscattering at 532 and 1,064 nm (Liu et al., 2009), and the layer temperatures are obtained from ancillary meteorological data from the Global Modeling and Assimilation Office. The cloud layer products are produced at three horizontal resolutions: 1/3, 1, and 5 km. In this study, we use products at 5 km for consistency with the scale of the AHI level 2 cloud properties.

3. Methods

This study uses Himawari/AHI cloud properties to design the SWC detection algorithm. Then, the CALIPSO results, which are estimated based on the method of Hu et al. (2010), are taken as the true SWCs to validate the accuracy of this algorithm. Details on this method and evaluation are shown below.

3.1. The HSWC Algorithm

Droplets within a SWC can be frozen into ice crystals when below a certain temperature, which is known as homogeneous nucleation. The temperature change in SWCs triggers homogeneous nucleation. Therefore, we determine an appropriate temperature at which to detect SWCs. Given that from a high temperature (T_0) to a turning-point temperature (T_F) almost all SWCs are frozen, the freezing ratio is estimated as a function of the unit volume nucleation rate $J_i(T)$, the equilibrium melting temperature T , the cooling rate γ_c , and the droplet volume V_d (Pruppacher & Klett, 1997):

$$\int_{T_F}^{T_0} J_i(T) dT = 9.21 \frac{\gamma_c}{V_d} \quad (1)$$

The diameter of cloud droplets ranges from 10 to 20 μm , and, according to equation (1), the average freezing temperature is approximately -38 °C. The detailed process can be found in Pruppacher and Klett (1997). Whether SWCs in the liquid-phase experience homogeneous freezing or not depends on the temperature, droplet size (Vali et al., 2015), and cooling rate. Generally, larger droplets are related to a higher freezing temperature (Baran et al., 2003; Zhao et al., 2017).

Heterogeneous nucleation in the mixed phase is initiated by ice nuclei (INs) acted on by aerosol particles (Wallace & Hobbs, 2006); with the aid of INs, the nucleation process begins at a larger particle size; hence, cloud droplets are still capable of freezing without requiring a temperature as low as that required for homogeneous nucleation. SWC bulk densities are nucleated into ice under a series of freezing mechanisms (Khvorostyanov & Curry, 2005), including deposition, contact freezing, condensation freezing, and immersion freezing. During deposition nucleation, the freezing temperature increases with the increase in droplet diameter; therefore, SWCs present a complex temperature distribution threshold. Whether the IN is activated or not mainly depends on the temperature and supersaturation. However, supersaturation cannot be obtained from satellites. According to the above SWC microphysical process, the CPH, CTT, and CER need to be considered when the phase threshold method is applied to identify SWCs.

The CPH and CTT are indicators used for SWC identification. The complete glaciation of SWCs can occur through the Bergeron process (Baran et al., 2003), in which updrafts are not strong enough to maintain supersaturation (Korolev, 2008). Studies have investigated the CTT threshold to detect SWCs. In SWCs, when the temperature of large droplets reaches the homogeneous freezing threshold, the lowest temperatures are generally -19 (Ikeda et al., 2007) and -21 °C (Cober et al., 2001). Yorks et al. (2011) found that

Table 1
Cloud Properties Input Into the HSWC Algorithm and Their Thresholds

Properties	Value change	References
Cloud Phase	Liquid and mixed	Pruppacher and Klett (1997)
Cloud top temperature	0 to -38°C	Pruppacher and Klett (1997) and Yorks et al. (2011)
Cloud effective radius	1 to $50\ \mu\text{m}$	Rogers and Yau (1989) and Rosenfeld et al. (2006)
Cloud optical thickness	>1	Roskovensky et al. (2011)

Note. HSWC = Himawari-8 supercooled water cloud.

from the liquid to ice phase, the transition temperature was -20°C at an 8-km height. Similar to these previous studies, we adopted the CPH and CTT in our HSWC algorithm, with liquid and mixed-phase threshold values of 0 and -38°C , respectively, as shown in Table 1.

The CER has important effects on both homogeneous and ice nucleation. For adiabatic LWCs at -38°C , precipitation-sized particles whose radii were larger than $50\ \mu\text{m}$ were not detected under these supercooled conditions (Rosenfeld et al., 2006). It takes a long time for droplets to reach $50\ \mu\text{m}$ to initiate the collision-coalescence process (Rogers & Yau, 1989). We determined the CER distribution statistics from the airborne measurements of SWCs to analyze the variance in SWC frequency with the CER in liquid- and mixed-phase clouds (Figure 2). We find that the CER frequency in liquid-phase clouds is larger than that in mixed-phase clouds under the condition that the CER is smaller than approximately $18\ \mu\text{m}$. When $\text{CER} > 18\ \mu\text{m}$, the SWC frequency in mixed-phase clouds begins to account for a greater proportion. Thus, in addition to the CPH and CTT, the HSWC algorithm also uses the CER retrieved from the Himawari-8 2.3- μm channel.

SWC pixels are often found in thick clouds. The detection of potential SWC pixels in clouds is related to the cloud physical thickness (Roskovensky et al., 2011). Minnis et al. (1995) estimated the cloud physical thickness using the COT and CTT. The estimated cloud physical thickness increases with COT at the same CTT. Similar to Roskovensky et al. (2011), we use a minimum threshold value of 1 for the COT to detect SWCs with our HSWC algorithm.

In summary, the HSWC algorithm uses CPH, CER, CTT, and COT as four criteria to distinguish SWC regions (Table 1). In accordance with the flow chart in Figure 3, we first select two CPHs, including (1) liquid phase and (2) mixed phase, and then interpret the SWCs in reference to corresponding thresholds of CER,

CTT, and COT. Thus, (1) the CTT is 0 to -20°C and the CER is 1 to $18\ \mu\text{m}$; (2) the CTT is -20 to -38°C , and the CER is 18 to $50\ \mu\text{m}$. Both groups of thresholds should meet the condition of COT greater than 1. To test the validity of the CER and mixed phase in the CPH tests, we perform a sensitivity analysis in this study. Detailed information is presented in section 4.1.

3.2. Validation Method

To verify the HSWC algorithm, we use the (Hu et al., 2010) algorithm to obtain simultaneous lidar results. The CALIPSO cloud temperature is used to estimate the SWC fractions in the column (Hu et al., 2010).

$$f(T) = \frac{1}{1 + e^{-p(T)}} \quad (2)$$

Hu et al. (2010) parameterized the relationship between the SWC fraction and cloud temperature with equation (2). Here, $p(T)$ represents a polynomial fitting function for the relationship between the observed SWC fraction $f(T)$ and temperature (T). Details of the computing method can be found in Hu et al. (2010). The least square fit of $p(T)$ for the CALIPSO midlayer cloud temperature (T_{mid}) is

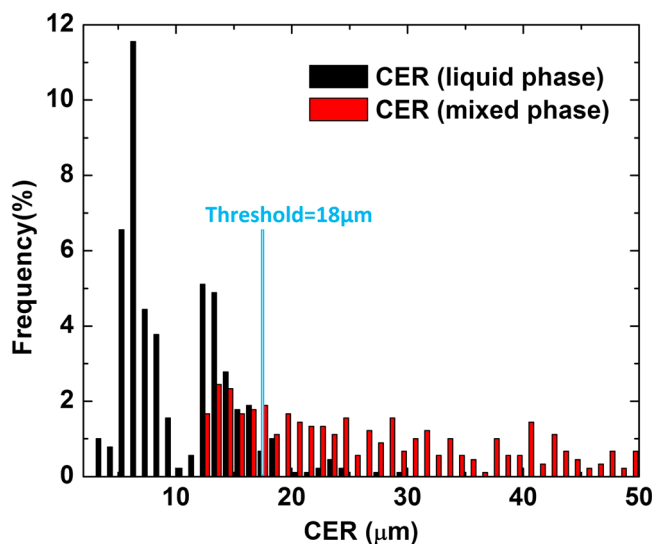


Figure 2. Comparison of the cloud effective radius (CER) frequency distributions in liquid- and mixed-phase clouds based on airborne measurements of supercooled water cloud.

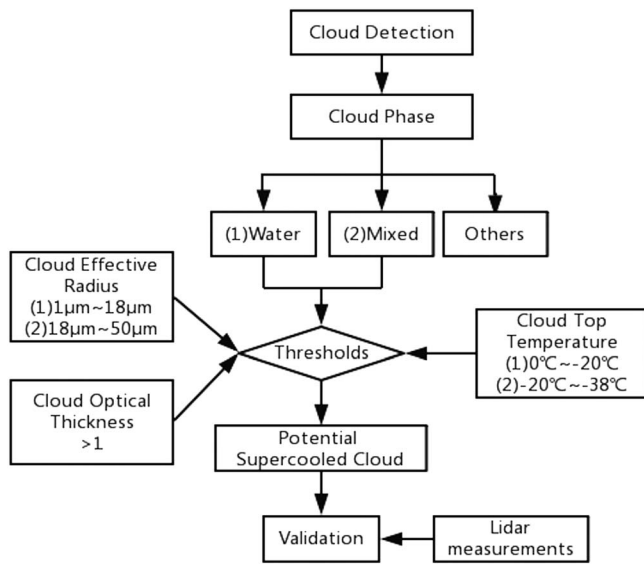


Figure 3. The Himawari-8 SWC algorithm flow chart using Himawari-8/Advanced Himawari Imager cloud products.

$$p(T_{\text{mid}}) = 5.3608 + 0.4025T_{\text{mid}} + 0.08387T_{\text{mid}}^2 + 0.007182T_{\text{mid}}^3 + 2.39 \times 10^{-4}T_{\text{mid}}^4 + 2.87 \times 10^{-6}T_{\text{mid}}^5 \quad (3)$$

The CALIPSO results are reliable because the relation between the SWC fraction and midlayer temperature shows very few seasonal variations (Hu et al., 2010). The detection can be biased toward higher-altitude clouds because only the top cloud layer is considered. Therefore, the SWC fraction is underestimated. However, most SWC areas are in high-latitude regions, whereas equations (2) and (3) weight all observations equally (Hu et al., 2010), which results in many more SWCs observed by CALIPSO.

The midlayer cloud temperature is originally estimated from the CALIOP cloud height and GEOS-5 temperature profiles (Hu et al., 2010). In this study, we used the CALIPSO cloud layer midtemperature instead to generate SWCs with equations (2) and (3). To include more CALIPSO SWC detections and guarantee precision, we select cases with the SWC fraction greater than 80% as the true SWCs. The CALIOP orbit track passes over the study area (Figure 1) at approximately 3:00 to 7:00 UTC every day. This track passes over the Tibetan Plateau and Indian Ocean at 7:00 UTC. Therefore, we obtained the AHI measurements at 7:00 UTC for consistency with the CALIPSO results.

In this study, the accuracy of the SWC detection by the HSWC algorithm is evaluated based on the CALIPSO results. Notably, the lidar and AHI observations are sensitive to cloud top microphysical information (Hu et al., 2010), which demonstrates the legitimacy of the validation method. The false alarm rate (FAR; Mace et al., 1998) and hit rate (HR; Liu et al., 2010; Mace et al., 1998) are shown in equations (4) and (5) to examine the performance of the detection results. The FAR represents the fraction of pixels that are misclassified as SWCs, and the HR suggests the probability of correctly identifying SWCs.

$$\text{False alarm rate} = \frac{\text{AHI}_{\text{swc}} \& \text{CALIPSO}_{\text{non-swc}}}{\text{AHI}_{\text{swc}}} \quad (4)$$

$$\text{Hit rate} = \frac{N_{\text{swc}} + N_{\text{non-swc}}}{N_{\text{collocated}}} \quad (5)$$

where AHI_{swc} is the number of SWC pixels in AHI SWC detections and $\text{CALIPSO}_{\text{non-swc}}$ is the number of non-SWC pixels in CALIPSO results. “&” indicates the pixels in agreement. N_{swc} is the number of SWC pixels in agreement, $N_{\text{non-swc}}$ is the number of non-SWC pixels in agreement, and $N_{\text{collocated}}$ is the total number of collocated pixels.

4. Results and Discussion

4.1. Determination of the SWC Tests

Previous studies used the liquid phase in the CPH and CTT to detect SWCs. Introducing the COT is an improvement when identifying SWCs. The analyses mentioned above indicate that SWC detection is related to the CER and mixed phase in the CPH. However, it remains unclear how the CER and mixed-phase tests could improve the performance of SWC detection. We design five different tests to validate the effectiveness of cloud properties mentioned above in identifying SWCs (Table 2). Test I is defined with two tests, including (1) the liquid phase and (2) the CTT, which is between 0 and -38°C , according to the GOES-R algorithm theoretical basis document. Test II includes the test of a COT larger than 1, which is similar to the MODIS SWC detection method developed by Roskovensky et al. (2011). Test III includes the test of a CER ranging from 1 to $50\ \mu\text{m}$. Test IV combines the four tests mentioned above. Test V includes the test for the mixed phase in the CPH, which is defined as (1) the liquid phase or mixed phase; (2) the CTT from 0 to -20°C and -20 to -38°C , respectively; (3) the CER from 1 to $18\ \mu\text{m}$ and 18 to $50\ \mu\text{m}$, respectively; and (4) a COT larger than 1.

Table 2
Five Tests to Validate the Effectiveness of Cloud Properties in Identifying SWCs

Test	Properties	References		
Test I	Liquid phase and CTT	Pavolonis (2010)		
Test II	Liquid phase, CTT, and COT	Roskovensky et al. (2011)		
Test III	Liquid phase, CTT, and CER	The distribution of SWCs is sensitive to CER values		
Test IV	Liquid phase, CTT, COT, and CER	Test II+ and Test III		
Test V	Liquid and mixed phase, CTT, COT, and CER	SWCs may appear in mixed-phase clouds identified by satellites.		
High-latitude regions	No. observations	HR (%)	No. observations	FAR (%)
Test I	393	84.48	145	46.21
Test II	393	95.17	103	24.27
Test III	393	99.24	87	6.90
Test IV	393	99.24	87	6.90
Test V	393	100	84	2.38
Ocean	No. observations	HR (%)	No. observations	FAR (%)
Test I	571	74.61	230	76.09
Test II	571	80.74	195	71.28
Test III	571	92.64	127	40.16
Test IV	571	92.64	127	40.16
Test V	571	99.82	86	1.16
Land	No. observations	HR (%)	No. observations	FAR (%)
Test I	234	68.80	139	60.43
Test II	234	75.64	123	48.78
Test III	234	83.76	104	39.42
Test IV	234	84.62	102	38.24
Test V	234	89.32	91	28.57
The entire CALIOP orbit track	No. observations	HR (%)	No. observations	FAR (%)
Test I	2674	76.07	1331	59.05
Test II	2674	85.19	1087	47.65
Test III	2674	91.14	928	32.97
Test IV	2674	91.44	920	32.39
Test V	2674	96.19	793	16.77

Note. The HR and FAR of the SWC detection tests I–V over high-latitude regions, ocean, land, and the entire CALIPSO orbit track at 3:00 UTC on 28 August 2017, based on CALIPSO results. SWC = supercooled water cloud; CTT = cloud top temperature; COT = cloud optical thickness; CER = cloud effective radius; HR = hit rate; FAR = false alarm rate; CALIOP = Cloud-Aerosol Lidar with Orthogonal Polarization.

Five tests are applied to the Himawari-8 cloud property data at 3:00 UTC on 28 August 2017. To analyze the typical regions in Figure 1, SWC pixels detected by the three algorithms over high-latitude regions, oceans, and lands are presented in Figure 4. Among the three different regions, the land region is between 60°S and 30°S, where SWCs affected by atmospheric dynamics and aerosols (Li et al., 2017) introduce uncertainties in the surface flux estimation and climate model simulation.

Quantitative analyses on the accuracies of the five tests referencing the CALIPSO results are recorded in Table 2. For the entire CALIOP orbit track, SWC pixels designated by test III have a better agreement with the CALIPSO results than the SWC detection results of test I, with HR values of 91.14% and 76.07%, respectively. The FAR values for the two tests are 32.97% and 59.05%, respectively. These results indicate that the CER test improves the accuracy of SWC detection. The SWC detection results via tests V and IV have HR values of 96.19% and 91.44%, respectively, with corresponding FAR values of 32.39% and 16.77%. These results confirm the efficiency of the mixed-phase test in the CPH. Furthermore, comparing tests I

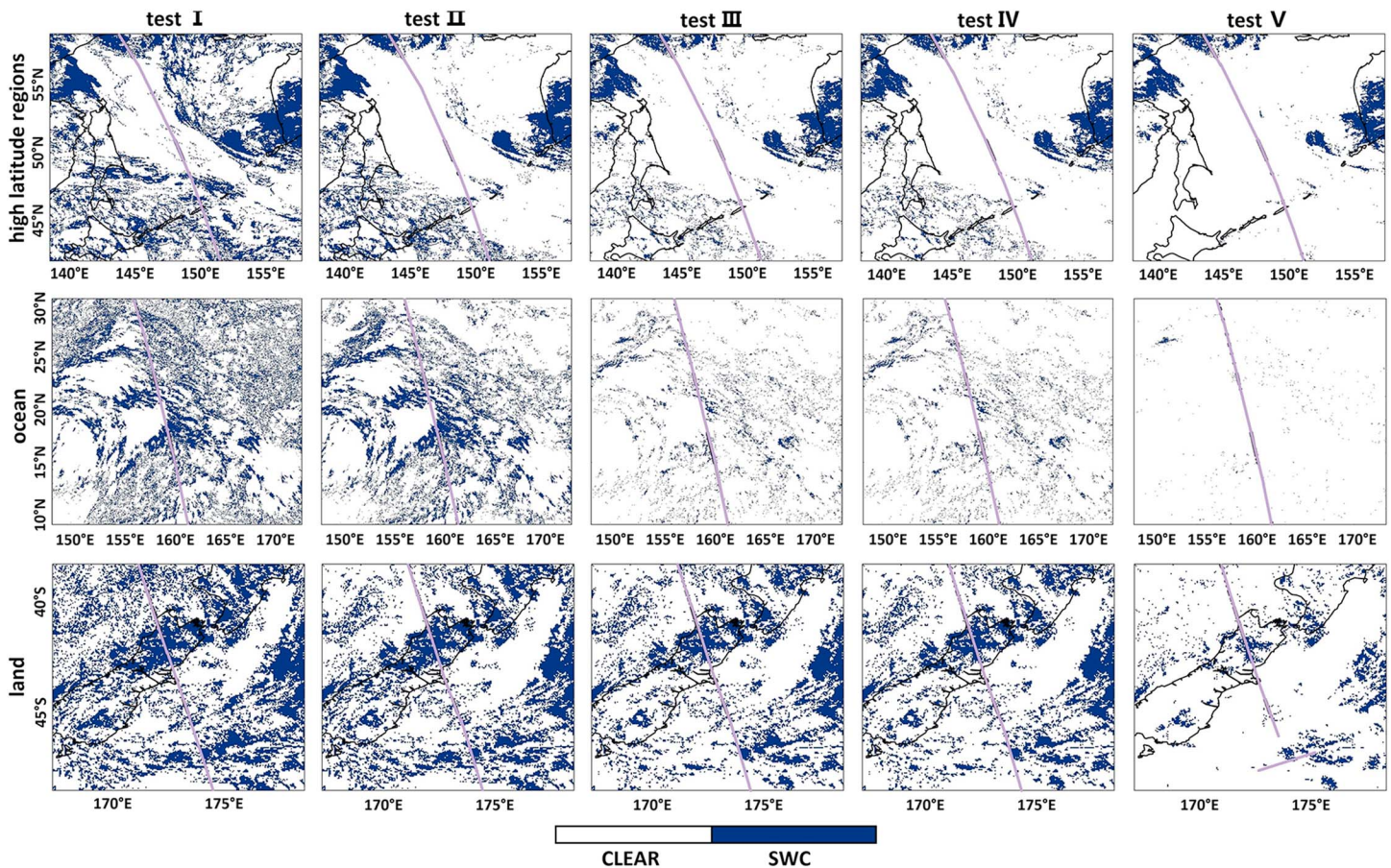


Figure 4. Supercooled water cloud (SWC) detection results of the tests I–V (every column) over high-latitude regions, ocean, and land (every line) at 3:00 UTC on 28 August 2017. The purple dashed line represents the Cloud-Aerosol Lidar with Orthogonal Polarization orbit track.

and II and tests III and IV shows increasing HR values of 9.12% and 0.3% and decreasing FAR values of 11.4% and 15.62%, respectively, which proves that the COT test is necessary. As illustrated in Figure 4, SWCs over three different regions are overestimated by test I. In contrast, tests III and V, which include the CER or mixed-phase tests, reduce the probability of misinterpreting small-droplet liquid clouds as SWCs and accurately identify SWCs in mixed-phase clouds. This result can be explained by the effective radius of SWCs, which is a sensitive factor for the distribution of SWC pixels that may appear in mixed-phase clouds.

Test III, which involves the CER, has a better enhancement than test V (involving the mixed phase in CPH) over the three different regions. These two tests both have the greatest improvements over the oceans, with increasing HR values of 18.03% and 7.18%, respectively. Over land, compared with test I, test III has the weakest improvements, with an increase in the HR of 14.96%. This result may be due to the inversion imprecision of cloud properties input into the algorithms over land, which are larger than those over the ocean. Over high-latitude regions, compared with test IV, test V has the weakest improvements, with a decrease in the FAR of 4.52%, because a large portion of SWCs appears over high-latitude regions, and the SWC detection precision originally approaches 100%. Therefore, adding tests involving the CER and mixed phase in the CPH improves the accuracy of detecting SWCs. The number of participating pixels is recorded in Table 2.

4.2. Spatial and Vertical Algorithm Results

As illustrated in Figures 5a and 5b, the CER in mixed clouds is generally larger than that in liquid clouds. The threshold design of the HSWC algorithm involves the characteristics of cloud microphysics. The

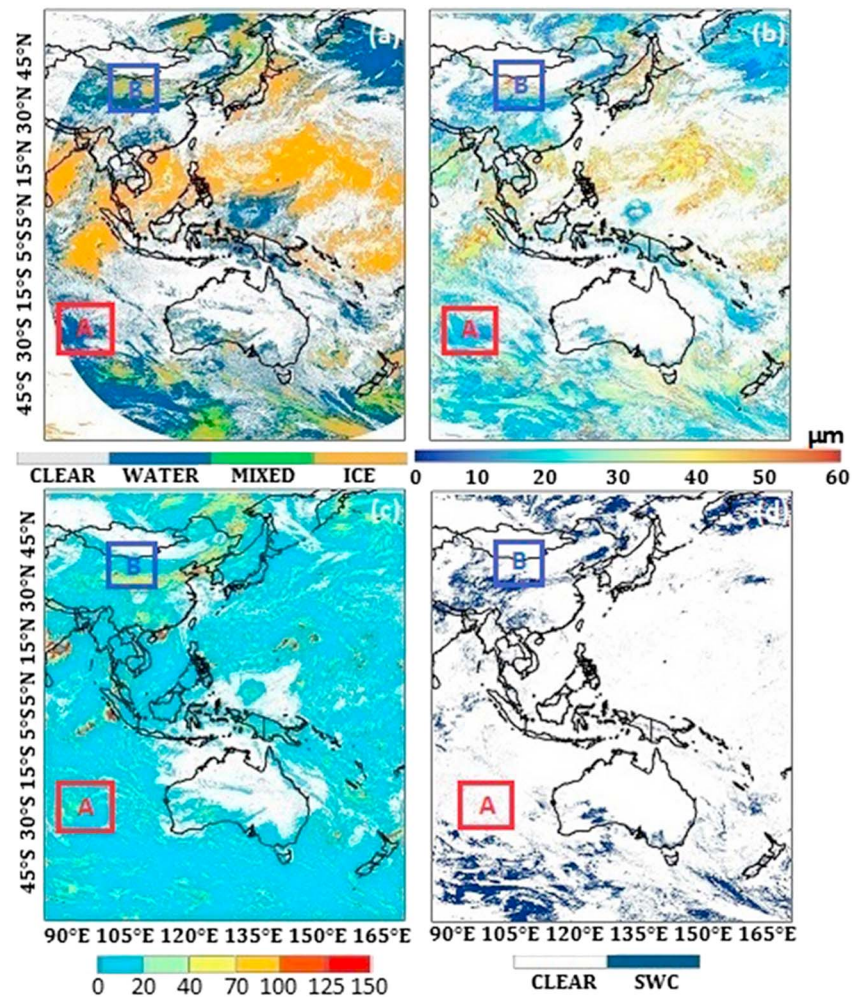


Figure 5. (a) Cloud phase, (b) cloud effective radius, (c) cloud optical thickness derived from Himawari-8 cloud products, and (d) supercooled water cloud results of the Himawari-8 supercooled water cloud algorithm at 3:00 UTC on 28 August 2017.

ocean in box A in Figure 5a is covered with water clouds; however, the effective radii in this box are larger than $20 \mu\text{m}$. Hence, non-SWCs in Figure 5d are detected according to the thresholds. Mixed-phase and ice clouds exist in the region of box B, where the effective radii are approximately $40\text{--}50 \mu\text{m}$ and the COT in Figure 5c ranges from 0 to 20. With the HSWC algorithm, a small number of SWCs are detected. The SWC detection results are consistent with the spatial distribution characteristics of the CPH, CER and COT.

As illustrated in the CALIPSO results and SWC results of the HSWC algorithm in the top graphs of Figures 6a and 6b, two cases (94.58% and 99.05%) with SWC or clear pixels are correctly identified by the HSWC algorithm at 7:00 UTC on 9 January and 17 May 2017, respectively. Clear pixels account for a large proportion of the total collocated pixels and match well with the CALIPSO results, which demonstrates good detection accuracy. The FAR values for the two cases were 19.24% and 4.31%, respectively. In Figures 6a and 6b, the SWCs observed by the AHI and CALIPSO are consistent with each other from 50°S to 40°S and 20°S along the orbit. This result confirms that the HSWC algorithm performs well in detecting SWCs over oceans. For the CALIPSO results at 55°S along the CALIOP orbit track in Figure 6a, the CPH is mainly a liquid phase, the CTT is between 0 and -20°C , the radii are from 10 to $15 \mu\text{m}$, and the COT is from 10 to 20, which meets the threshold settings for the HSWC algorithm. This result indicates that the CALIPSO results are consistent with the spatial distributions of CPH, CTT, CER, and COT. Clouds with COTs ranging from 10 to 40 represent a concentrated area where SWCs exist.

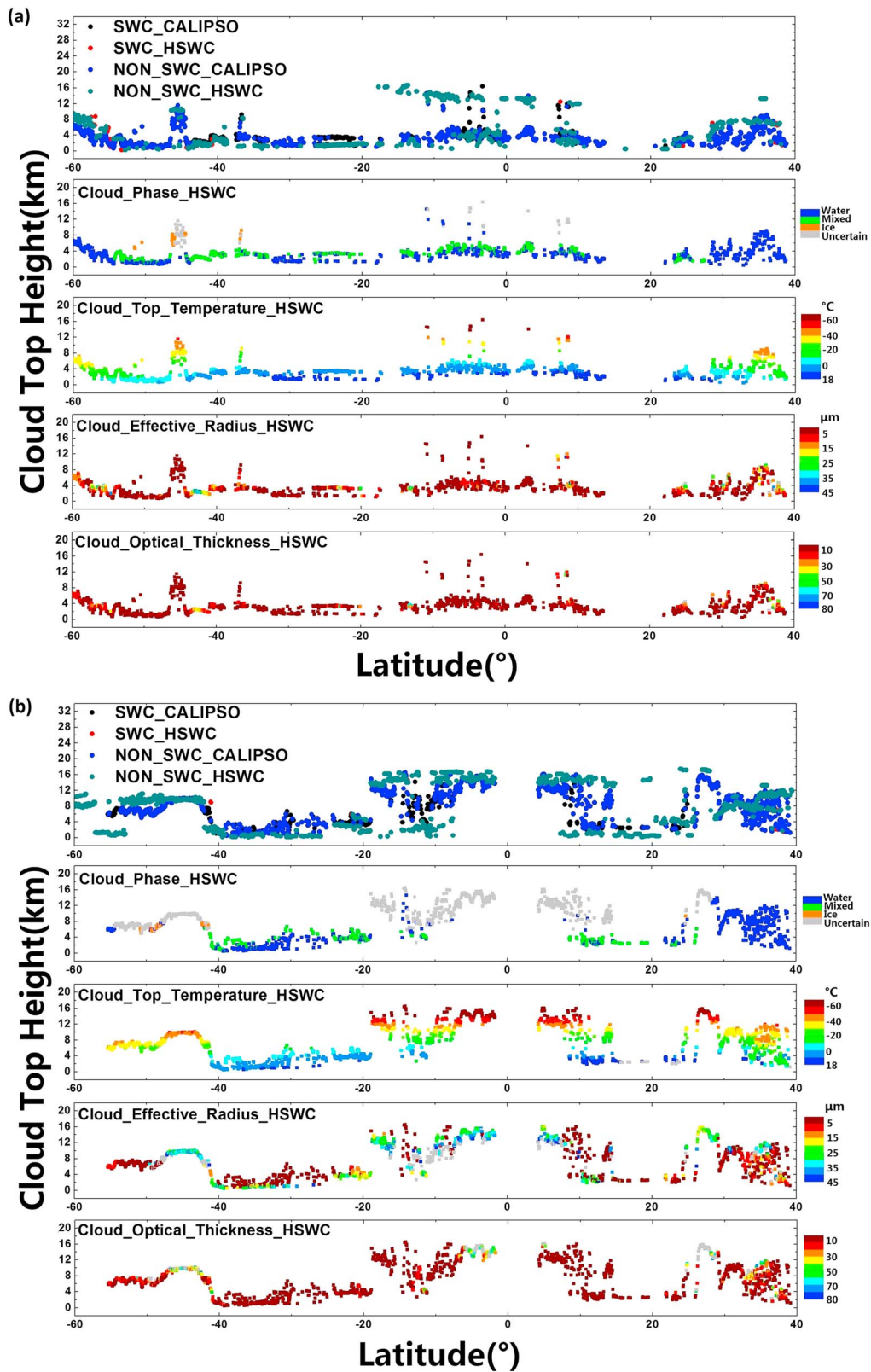


Figure 6. CALIPSO results and SWC results of the HSWC algorithm, respectively; cloud phase, cloud top temperature, cloud effective radius, and cloud optical thickness derived from Himawari-8 cloud products at 7:00 UTC on (a) 9 January and (b) 17 May 2017. The results related to Himawari-8 satellite match with the CALIOP orbit track. CALIPSO = Cloud-Aerosol Lidar and Infrared Pathfinder Satellite Observations; SWC = supercooled water cloud; HSWC = Himawari-8 SWC; CALIOP = Cloud-Aerosol Lidar with Orthogonal Polarization.

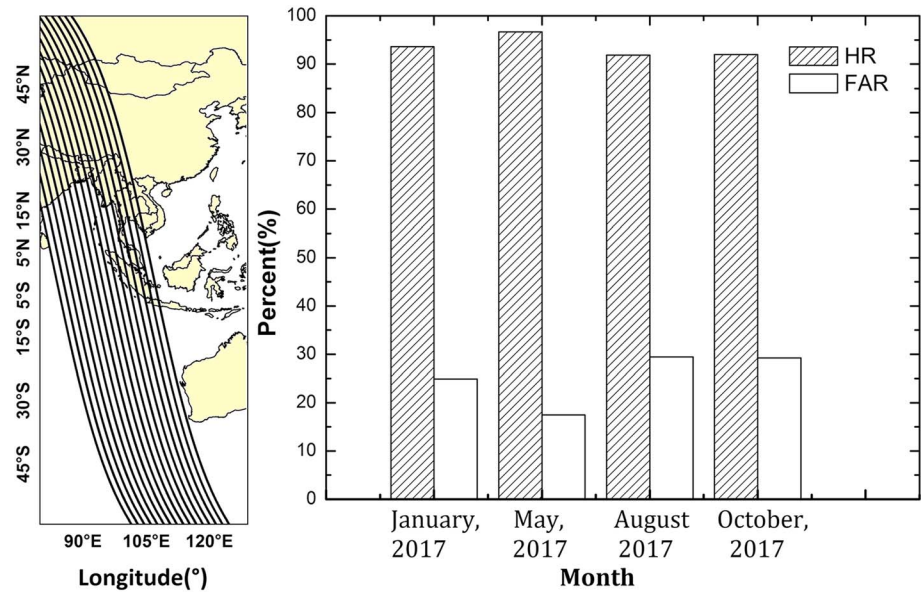


Figure 7. The black lines in the left image represent the track of Cloud-Aerosol Lidar and Infrared Pathfinder Satellite Observations results in Figure 8. The histogram in the right graph shows hit rate (HR) and false alarm rate (FAR) values for the Himawari-8 supercooled water cloud algorithm for January, May, August, and October in 2017.

4.3. Comparison With the CALIPSO Observations

Furthermore, we compared the HSWC algorithm SWC results with the simultaneous CALIPSO results over the entire study area. We selected January, May, August, and October of 2017 to represent the four seasons (a portion of CALIPSO observations in April and July are missing). As illustrated in Figure 7, the SWC results estimated from the HSWC algorithm well match the CALIPSO results, with average HR and FAR values of 93.52% and 25.27%, respectively. A number of pixels used in the comparison are presented in Table 3. For the months of January, May, August, and October in 2017, the average HR values of the SWC pixels via the HSWC algorithm were 93.60%, 96.69%, 91.86%, and 91.97%, and the FAR values were 24.89%, 17.47%, 29.44%, and 29.22%, respectively.

A daily comparison between the CALIPSO results and SWC results via the HSWC algorithm along the CALIPSO orbit track during the 4 months representing the four seasons was conducted to evaluate the performance of the SWC detection (Figure 8). Compared with the CALIPSO results, the AHI yielded more SWC pixels during spring and summer than during autumn and winter. For example, the average FAR via the SWC results from the AHI was less than 28% during spring and summer, whereas the values for autumn and winter exceeded 31%. The SWC detection misclassifies snow or ice areas as SWC clouds, which is related to the increase in ground snow and ice in middle- to high-latitude regions during autumn and winter (Shang et al., 2018). The HR and FAR fluctuated at the monthly scale. Further investigation of the SWC detection bias on 14 August and 15 October 2017, showed misclassified clear pixels as SWC pixels over oceans at low altitudes. This result indicates that the HSWC algorithm products show good agreement with the CALIPSO results.

Table 3

The HR and FAR of the HSWC Algorithm for January, May, August, and October in 2017 based on CALIPSO Results

Period	No. observations	HR (%)	FAR (%)
January 2017	94,160	93.60	24.89
May 2017	79,932	96.69	17.47
August 2017	73,222	91.86	29.44
October 2017	89,371	91.97	29.22
Total	336,685	93.52	25.27

Note. HR = hit rate; FAR = false alarm rate; HSWC = Himawari-8 supercooled water cloud; CALIPSO = Cloud-Aerosol Lidar and Infrared Pathfinder Satellite Observations.

Multilayer cloud systems are defined as two or more cloud layers at different altitudes simultaneously present over the same location (Tian & Curry, 1989). The multilayer cloud fractions are approximately 27% at the global scale (Wylie et al., 2007). Typical high-value centers of multilayer clouds occur over the tropics and midlatitudes (Li et al., 2015). The existence of overlapping cloud layers, such as ice-phase clouds, may obscure the lower-level clouds from view of Himawari-8 (a passive

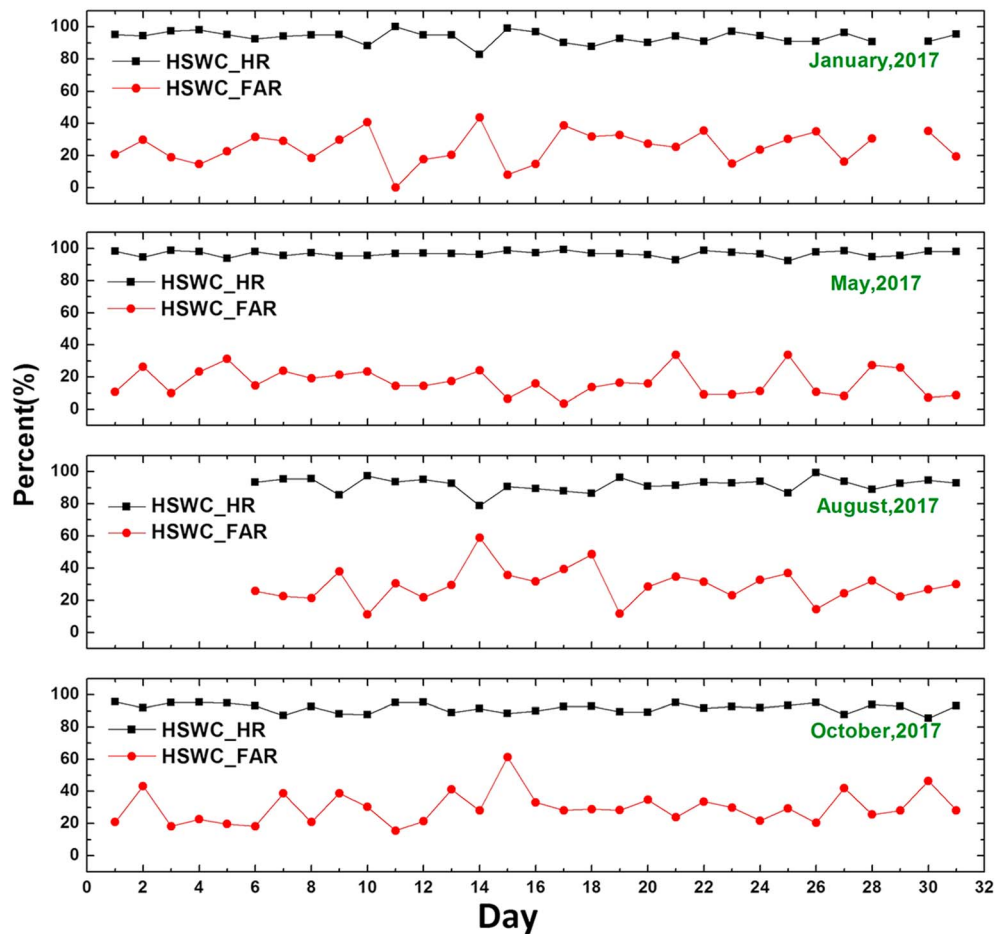


Figure 8. Hit rate (HR) and false alarm rate (FAR) values for the Himawari-8 supercooled water cloud (HSWC) algorithm for January, May, August, and October in 2017; the values were calculated based on Cloud-Aerosol Lidar and Infrared Pathfinder Satellite Observations results.

satellite), which results in the underestimation of CTT. The occurrence of multilayer clouds introduces errors into the HSWC algorithm, and we can use a neural network to optimize the algorithm.

There are also limitations to our evaluations in the following aspects. (1) For mixed clouds, the detection accuracy tends to decrease as the CER value increases. The HSWC algorithm has problems in SWC detection for large cloud droplets, which may be caused by difficulties in discriminating ice particles and SWC droplets in mixed clouds (Hirst et al., 2001). (2) The SWC results from the HSWC algorithm are validated by the CALIPSO results along the orbit track, which cannot provide a wide range of verification data. (3) From the satellite field of view, high-level ice clouds may overlap SWCs and reduce the ability to detect them (Smith et al., 2000).

5. Conclusion

The previous SWC detection method fails to achieve large-scale SWCs with high frequency and easily misclassifies cold clouds as SWCs. Based on the determination of the SWC tests showing that the distribution of SWCs is sensitive to CER values and that SWCs may appear in mixed-phase clouds identified by satellites, we proposed the HSWC algorithm by adding the CER and mixed-phase tests. This algorithm is applied to the Himawari-8 satellite CPH, CTT, CER, and COT products to obtain the potential SWC distribution and is needed for meteorological and disaster forecasting.

To test the validity of the CER and mixed-phase tests, we developed a sensitivity analysis in this study. At 3:00 UTC on 28 August 2017, the CER and mixed-phase tests improved the performance of SWC

detection by 15.07% and 4.75%, respectively. Based on the discussion and in contrast with the GOES-R and MODIS SWC testing methods without using the CER and mixed-phase tests, the HSWC algorithm can reduce the probability of interpreting small liquid cloud droplets as SWCs and correctly identify SWCs in mixed-phase clouds. Further validation with the CALIPSO results indicates that the proposed algorithm is reliable for detecting SWCs, with HR and FAR values of 93.52% and 25.27%, respectively. The HSWC algorithm provides the basis for the scientific implementation of artificial rain.

This HSWC algorithm also has limits. (1) The detection accuracy decreases with the increase in CER, which is related to misinterpreting ice particles as SWC droplets. (2) This algorithm may misclassify clear pixels as SWC pixels over oceans and has weak SWC detection ability over land, which is due to the bias from the retrieval of cloud properties. (3) From the view of the satellite, high-level ice clouds may overlap SWCs and result in the underestimation of CTT, which introduces errors into the SWC detection ability. In the future, we can use a neural network to optimize the algorithm. For validating our algorithm, (1) a layer of a mixed-phase cloud can be misidentified as either a water or ice cloud, and the latter may result in the underestimation of the CALIPSO SWC results; (2) verification data for SWC detection are rare and mostly include airborne, radiosonde, and lidar measurements with microregional or transitory time characteristics, which cause uncertainties when evaluating the algorithm accuracy.

Acknowledgments

This work was jointly supported by National Natural Science Foundation of China (Grants 41771395, 61261030, 41501398, and 41701406), China National Key Research and Development Plan Project (2018YFA0605400). The Himawari-8 data, provided by Meteorological Satellite Center (MSC) of the Japan Meteorological Agency (JMA), are available from the JAXA website (<http://www.eorc.jaxa.jp/ptree/index.html>). The Himawari-8 products are produced and distributed by the Japan Aerospace Exploration Agency (JAXA). The authors are very grateful to JAXA and JMA for the documents and data. The authors are thankful for flight observations from the Chinese Academy of Meteorological Science. We thank Chunyang Zhu from the China University of Petroleum for helping analyzing the cloud microphysics process. The authors declare that they have no competing interests.

References

- Alexandrov, M. D., Cairns, B., van Diedenhoven, B., Ackerman, A. S., Wasilewski, A. P., McGill, M. J., et al. (2016). Polarized view of supercooled liquid water clouds. *Remote Sensing of Environment*, *181*, 96–110. <https://doi.org/10.1016/j.rse.2016.04.002>
- Baran, A. J., Havemann, S., Francis, P. N., & Watts, P. D. (2003). A consistent set of single-scattering properties for cirrus cloud: Tests using radiance measurements from a dual-viewing multi-wavelength satellite-based instrument. *Journal of Quantitative Spectroscopy and Radiative Transfer*, *79–80*, 549–567. [https://doi.org/10.1016/S0022-4073\(02\)00307-2](https://doi.org/10.1016/S0022-4073(02)00307-2)
- Bellucci, M., Vernillo, P., Auletta, A., Esposito, B. M., Marrazzo, M., Ferrigno, F., & Crepin, J. P. (2007). SONACA icing test campaign on a 2D model at CIRA IWT. In *Asia Pacific Automotive Engineering Conference* (p. 48003943). The Angels: SAE International.
- Bessho, K., Date, K., Hayashi, M., Ikeda, A., Imai, T., Inoue, H., et al. (2016). An introduction to Himawari-8/9—Japan's new-generation geostationary meteorological satellites. *Journal of the Meteorological Society of Japan Series II*, *94(2)*, 151–183. <https://doi.org/10.2151/jmsj.2016-009>
- Choi, Y. S., Lindzen, R. S., Ho, C. H., & Kim, J. (2010). Space observations of cold-cloud phase change. *Proceedings of the National Academy of Sciences of the United States of America*, *107(25)*, 11,211–11,216. <https://doi.org/10.1073/pnas.1006241107>
- Cober, S. G., Isaac, G. A., & Strapp, J. W. (2001). Characterizations of aircraft icing environments that include supercooled large drops. *Journal of Applied Meteorology*, *40(11)*, 1984–2002. [https://doi.org/10.1175/1520-0450\(2001\)040<1984:coaie>2.0.co;2](https://doi.org/10.1175/1520-0450(2001)040<1984:coaie>2.0.co;2)
- Ellrod, G., & Nelson, J. P. (1996). *Remote sensing of aircraft icing regions using GOES multispectral imager data*. Paper Presented at Preprints 15th Conference on Weather Analysis and Forecasting, Norfolk, VA.
- Garrett, T. J., & Zhao, C. (2006). Increased Arctic cloud longwave emissivity associated with pollution from mid-latitudes. *Nature*, *440(7085)*, 787–789. <https://doi.org/10.1038/nature04636>
- Hirst, E., Kaye, P. H., Greenaway, R. S., Field, P., & Johnson, D. W. (2001). Discrimination of micrometre-sized ice and super-cooled droplets in mixed-phase cloud. *Atmospheric Environment*, *35(1)*, 33–47. [https://doi.org/10.1016/S1352-2310\(00\)00377-0](https://doi.org/10.1016/S1352-2310(00)00377-0)
- Hogan, R. J., Behera, M. D., O'Connor, E. J., & Illingworth, A. J. (2004). Estimate of the global distribution of stratiform supercooled liquid water clouds using the LITE lidar. *Geophysical Research Letters*, *31*, L05106. <https://doi.org/10.1029/2003GL018977>
- Hogan, R. J., Illingworth, A. J., O'Connor, E. J., & PoirasBaptista, J. P. V. (2003). Characteristics of mixed-phase clouds. II: A climatology from ground-based lidar. *Quarterly Journal of the Royal Meteorological Society*, *129(592)*, 2117–2134. <https://doi.org/10.1256/qj.01.209>
- Houze, R. A., Hobbs, P. V., Herzegh, P. H., & Parsons, D. B. (1979). Size distributions of precipitation particles in frontal clouds. *Journal of the Atmospheric Sciences*, *36(1)*, 156–162. [https://doi.org/10.1175/1520-0469\(1979\)036<0156:sdoppi>2.0.co;2](https://doi.org/10.1175/1520-0469(1979)036<0156:sdoppi>2.0.co;2)
- Hu, Y., Rodier, S., Xu, K.-M., Sun, W., Huang, J., Lin, B., et al. (2010). Occurrence, liquid water content, and fraction of supercooled water clouds from combined CALIOP/IIR/MODIS measurements. *Journal of Geophysical Research*, *115*, D00H34. <https://doi.org/10.1029/2009JD012384>
- Hu, Y., Vaughan, M., Liu, Z., Lin, B., Yang, P., Flittner, D., et al. (2007). The depolarization—Attenuated backscatter relation: CALIPSO lidar measurements vs. theory. *Optics Express*, *15(9)*, 5327–5332. <https://doi.org/10.1364/oe.15.005327>
- Hu, Y., Winker, D., Vaughan, M., Lin, B., Omar, A., Trepte, C., et al. (2009). CALIPSO/CALIOP cloud phase discrimination algorithm. *Journal of Atmospheric and Oceanic Technology*, *26(11)*, 2293–2309. <https://doi.org/10.1175/2009jtecha1280.1>
- Ikeda, K., Rasmussen, R. M., Hall, W. D., & Thompson, G. (2007). Observations of freezing drizzle in extratropical cyclonic storms during IMPROVE-2. *Journal of the Atmospheric Sciences*, *64(9)*, 3016–3043. <https://doi.org/10.1175/jas3999.1>
- Kawamoto, K., Nakajima, T., & Nakajima, T. Y. (2001). A global determination of cloud microphysics with AVHRR remote sensing. *Journal of Climate*, *14(9)*, 2054–2068. [https://doi.org/10.1175/1520-0442\(2001\)014<2054:agdocm>2.0.co;2](https://doi.org/10.1175/1520-0442(2001)014<2054:agdocm>2.0.co;2)
- Khvorostyanov, V. I., & Curry, J. A. (2005). The theory of ice nucleation by heterogeneous freezing of deliquescent mixed CCN. Part II: Parcel model simulation. *Journal of the Atmospheric Sciences*, *62(2)*, 261–285. <https://doi.org/10.1175/jas-3367.1>
- King, M. D., Tsay, S.-C., Platnick, S. E., Wang, M., & Liou, K.-N. (1997). *Cloud retrieval algorithms for MODIS: Optical thickness, effective particle radius, and thermodynamic phase*, MODIS algorithm theoretical basis document ATBDMOD-05. Greenbelt, MD: NASA Goddard Space Flight Center.
- Korolev, A. V. (2008). Rates of phase transformations in mixed-phase clouds. *Quarterly Journal of the Royal Meteorological Society*, *134(632)*, 595–608. <https://doi.org/10.1002/qj.230>
- Letu, H., Ishimoto, H., Riedi, J., Nakajima, T. Y., Labonnote, L. C., Baran, A. J., et al. (2016). Investigation of ice particle habits to be used for ice cloud remote sensing for the GCOM-C satellite mission. *Atmospheric Chemistry and Physics*, *16(18)*, 12,287–12,303. <https://doi.org/10.5194/acp-16-12287-2016>

- Letu, H., Nagao, T. M., Nakajima, T. Y., & Matsumae, Y. (2014). Method for validating cloud mask obtained from satellite measurements using ground-based sky camera. *Applied Optics*, *53*(31), 7523–7533. <https://doi.org/10.1364/AO.53.007523>
- Letu, H., Nagao, T. M., Nakajima, T. Y., Riedi, J., Ishimoto, H., Baran, A. J., et al. (2018). Ice cloud properties from Himawari-8/AHI next-generation geostationary satellite: Capability of the AHI to monitor the DC cloud generation process. *IEEE Transactions on Geoscience and Remote Sensing*, 1–11. <https://doi.org/10.1109/TGRS.2018.2882803>
- Li, J., Huang, J., Stamnes, K., Wang, T., Lv, Q., & Jin, H. (2015). A global survey of cloud overlap based on CALIPSO and CloudSat measurements. *Atmospheric Chemistry and Physics*, *15*(1), 519–536. <https://doi.org/10.5194/acp-15-519-2015>
- Li, J., Lv, Q., Zhang, M., Wang, T., Kawamoto, K., Chen, S., & Zhang, B. (2017). Effects of atmospheric dynamics and aerosols on the fraction of supercooled water clouds. *Atmospheric Chemistry and Physics*, *17*(3), 1847–1863. <https://doi.org/10.5194/acp-17-1847-2017>
- Lin, B., Minnis, P., Wielicki, B., Doelling, D. R., Palikonda, R., Young, D. F., & Uttal, T. (1998). Estimation of water cloud properties from satellite microwave, infrared and visible measurements in oceanic environments: 2. Results. *Journal of Geophysical Research*, *103*(D4), 3887–3905. <https://doi.org/10.1029/97JD02817>
- Lin, B., & Rossow, W. B. (1996). Seasonal variation of liquid and ice water path in nonprecipitating clouds over oceans. *Journal of Climate*, *9*(11), 2890–2902. [https://doi.org/10.1175/1520-0442\(1996\)009<2890:svolai>2.0.co;2](https://doi.org/10.1175/1520-0442(1996)009<2890:svolai>2.0.co;2)
- Liu, Y., Ackerman, S. A., Maddux, B. C., Key, J. R., & Frey, R. A. (2010). Errors in cloud detection over the Arctic using a satellite imager and implications for observing feedback mechanisms. *Journal of Climate*, *23*(7), 1894–1907. <https://doi.org/10.1175/2009jcli3386.1>
- Liu, Z., Vaughan, M., Winker, D., Kittaka, C., Getzewich, B., Kuehn, R., et al. (2009). The CALIPSO lidar cloud and aerosol discrimination: Version 2 algorithm and initial assessment of performance. *Journal of Atmospheric and Oceanic Technology*, *26*(7), 1198–1213. <https://doi.org/10.1175/2009jtecha1229.1>
- Luke, E. P., Kollias, P., & Shupe, M. D. (2010). Detection of supercooled liquid in mixed-phase clouds using radar Doppler spectra. *Journal of Geophysical Research*, *115*, D19201. <https://doi.org/10.1029/2009JD012884>
- Mace, G. G., Jakob, C., & Moran, K. P. (1998). Validation of hydrometeor occurrence predicted by the ECMWF model using millimeter wave radar data. *Geophysical Research Letters*, *25*(10), 1645–1648. <https://doi.org/10.1029/98GL00845>
- Minnis, P., Smith, W. L., Garber, D. P., Ayers, J. K., & Doelling, D. R. (1995). Cloud properties derived from GOES-7 for spring 1984 ARM intensive observing period using version 1.0.0 of ARM satellite data analysis program. NASA reference publication 1366. Hampton VA: NASA Langley Research Center.
- Murray, B. J., O'Sullivan, D., Atkinson, J. D., & Webb, M. E. (2012). Ice nucleation by particles immersed in supercooled cloud droplets. *Chemical Society Reviews*, *41*(19), 6519. <https://doi.org/10.1039/c2cs35200a>
- Nakajima, T. Y., & Nakajima, T. (1995). Wide-area determination of cloud microphysical properties from NOAA AVHRR measurements for fire and ASTEX regions. *Journal of the Atmospheric Sciences*, *52*(23), 4043–4059. [https://doi.org/10.1175/1520-0469\(1995\)052<4043:wadocm>2.0.co;2](https://doi.org/10.1175/1520-0469(1995)052<4043:wadocm>2.0.co;2)
- Nakajima, T. Y., Suzuki, K., & Stephens, G. L. (2010a). Droplet growth in warm water clouds observed by the A-train. Part I: Sensitivity analysis of the MODIS-derived cloud droplet sizes. *Journal of the Atmospheric Sciences*, *67*(6), 1884–1896. <https://doi.org/10.1175/2009jas3280.1>
- Nakajima, T. Y., Suzuki, K., & Stephens, G. L. (2010b). Droplet growth in warm water clouds observed by the A-train. Part II: A multisensor view. *Journal of the Atmospheric Sciences*, *67*(6), 1897–1907. <https://doi.org/10.1175/2010jas3276.1>
- Pavolonis, M. (2010). *GOES-R advanced baseline imager (ABI) algorithm theoretical basis document for cloud type and cloud phase*. Winconsin: NOAA.
- Pruppacher, H. R., & Klett, J. D. (1997). *Microphysics of clouds and precipitation*. Boston, MA: Kluwer Academy.
- Reisner, J., Rasmussen, R. M., & Bruintjes, R. T. (1998). Explicit forecasting of supercooled liquid water in winter storms using the MM5 mesoscale model. *Quarterly Journal of the Royal Meteorological Society*, *124*(548), 1071–1107. <https://doi.org/10.1256/smsqj.54803>
- Rogers, R. R., & Yau, M. K. (1989). *A short course in cloud physics*. New York, NY: Pergamon.
- Rosenfeld, D., Woodley, W. L., Krauss, T. W., & Makitov, V. (2006). Aircraft microphysical documentation from cloud base to anvils of hailstorm feeder clouds in Argentina. *Journal of Applied Meteorology and Climatology*, *45*(9), 1261–1281. <https://doi.org/10.1175/jam2403.1>
- Roskovensky, J. K., Ivey, I., Porch, W., Beavis, N., Hermann, R., & Silber, S. (2011). Cloud super-cooled liquid water estimation from satellite data. *The Journal of Weather Modification*, *43*(1), 64–82.
- Shang, H., Letu, H., Nakajima, T. Y., Wang, Z., Ma, R., Wang, T., et al. (2018). Diurnal cycle and seasonal variation of cloud cover over the Tibetan Plateau as determined from Himawari-8 new-generation geostationary satellite data. *Scientific Reports*, *8*(1), 1105. <https://doi.org/10.1038/s41598-018-19431-w>
- Smith, W. L., Minnis, P., Fleeger, C., Spangenberg, D., Palikonda, R., & Nguyen, L. (2012). Determining the flight icing threat to aircraft with single-layer cloud parameters derived from operational satellite data. *Journal of Applied Meteorology and Climatology*, *51*(10), 1794–1810. <https://doi.org/10.1175/jamc-d-12-057.1>
- Smith, W. L., Minnis, P., & Young, D. F. (2000). *An icing product derived from operational satellite data*. Paper Presented at AMS Ninth Conference on Aviation, Range, and Aerospace Meteorology, Orlando, FL.
- Tian, L., & Curry, J. A. (1989). Cloud overlap statistics. *Journal of Geophysical Research*, *94*(D7), 9925–9935. <https://doi.org/10.1029/JD094id07p09925>
- Vali, G., DeMott, P. J., Möhler, O., & Whale, T. F. (2015). Technical note: A proposal for ice nucleation terminology. *Atmospheric Chemistry and Physics*, *15*(18), 10,263–10,270. <https://doi.org/10.5194/acp-15-10263-2015>
- Wakimizu, K., Nishiyama, K., Suzuki, Y., Tomine, K., Yamazaki, M., Isimaru, A., et al. (2002). A low-level penetration seeding experiment of liquid carbon dioxide in a convective cloud. *Hydrological Processes*, *16*(11), 2239–2253. <https://doi.org/10.1002/hyp.1153>
- Wallace, J. M., & Hobbs, P. V. (2006). *Atmospheric science: An introductory survey*. Amsterdam, Netherlands: Elsevier Academic Press.
- Wang, Y., & Zhao, C. (2017). Can MODIS cloud fraction fully represent the diurnal and seasonal variations at DOE ARM SGP and Manus sites? *Journal of Geophysical Research: Atmospheres*, *122*, 329–343. <https://doi.org/10.1002/2016JD025954>
- Weidle, F., & Wernli, H. (2008). Comparison of ERA40 cloud top phase with POLDER-1 observations. *Journal of Geophysical Research*, *113*, D05209. <https://doi.org/10.1029/2007JD009234>
- Westbrook, C. D., & Illingworth, A. J. (2011). Evidence that ice forms primarily in supercooled liquid clouds at temperatures >−27 °C. *Geophysical Research Letters*, *38*, L14808. <https://doi.org/10.1029/2011GL048021>
- Wylie, D., Eloranta, E., Spinhirne, J. D., & Palm, S. P. (2007). A comparison of cloud cover statistics from the GLAS lidar with HIRS. *Journal of Climate*, *20*(19), 4968–4981. <https://doi.org/10.1175/jcli4269.1>
- Yao, B., Liu, C., Yin, Y., Zhang, P., Min, M., & Han, W. (2018). Radiance-based evaluation of WRF cloud properties over East Asia: Direct comparison with FY-2E observations. *Journal of Geophysical Research: Atmospheres*, *123*, 4613–4629. <https://doi.org/10.1029/2017JD027600>

- Yorks, J. E., Hlavka, D. L., Hart, W. D., & McGill, M. J. (2011). Statistics of cloud optical properties from airborne lidar measurements. *Journal of Atmospheric and Oceanic Technology*, 28(7), 869–883. <https://doi.org/10.1175/2011jtecha1507.1>
- Zhang, D., Wang, Z., & Liu, D. (2010). A global view of midlevel liquid-layer topped stratiform cloud distribution and phase partition from CALIPSO and CloudSat measurements. *Journal of Geophysical Research*, 115, D00H13. <https://doi.org/10.1029/2009JD012143>
- Zhao, C., & Garrett, T. J. (2015). Effects of Arctic haze on surface cloud radiative forcing. *Geophysical Research Letters*, 42, 557–564. <https://doi.org/10.1002/2014GL062015>
- Zhao, C., Liu, L., Wang, Q., Qiu, Y., Wang, Y., & Wu, X. (2017). MMCR-based characteristic properties of non-precipitating cloud liquid droplets at Naqu site over Tibetan Plateau in July 2014. *Atmospheric Research*, 190, 68–76. <https://doi.org/10.1016/j.atmosres.2017.02.002>
- Zhao, C., Qiu, Y., Dong, X., Wang, Z., Peng, Y., Li, B., et al. (2018). Negative aerosol-cloud re relationship from aircraft observations over Hebei, China. *Earth and Space Science*, 5, 19–29. <https://doi.org/10.1002/2017EA000346>
- Zhao, C., Xie, S., Klein, S. A., Protat, A., Shupe, M. D., McFarlane, S. A., et al. (2012). Toward understanding of differences in current cloud retrievals of ARM ground-based measurements. *Journal of Geophysical Research*, 117, D10206. <https://doi.org/10.1029/2011JD016792>